

Thermal conductivity of BN-C nanostructures

Alper Kinacı

Material Science and Engineering, Texas A&M University, College Station, Texas 77845-3122, USA

Justin B. Haskins

Artie McFerrin Department of Chemical Engineering, Texas A&M University, College Station, Texas 77845-3122, USA

Cem Sevik

Artie McFerrin Department of Chemical Engineering & Material Science and Engineering, Texas A&M University, College Station, Texas 77845-3122, USA and Advanced Technologies Research Center, Anadolu University, Eskisehir 26470, Turkey

Tahir Çağın*

Artie McFerrin Department of Chemical Engineering & Material Science and Engineering, Texas A&M University, College Station, Texas 77845-3122, USA

(Received 19 July 2012; revised manuscript received 16 August 2012; published 6 September 2012)

Chemical and structural diversity present in hexagonal boron nitride (*h*-BN) and graphene hybrid nanostructures provide avenues for tuning various properties for their technological applications. In this paper we investigate the variation of thermal conductivity (κ) of hybrid graphene/*h*-BN nanostructures: stripe superlattices and BN (graphene) dots embedded in graphene (BN) are investigated using equilibrium molecular dynamics. To simulate these systems, we have parametrized a Tersoff type interaction potential to reproduce the *ab initio* energetics of the B-C and N-C bonds for studying the various interfaces that emerge in these hybrid nanostructures. We demonstrate that both the details of the interface, including energetic stability and shape, as well as the spacing of the interfaces in the material, exert strong control on the thermal conductivity of these systems. For stripe superlattices, we find that zigzag configured interfaces produce a higher κ in the direction parallel to the interface than the armchair configuration, while the perpendicular conductivity is less prone to the details of the interface and is limited by the κ of *h*-BN. Additionally, the embedded dot structures, having mixed zigzag and armchair interfaces, affect the thermal transport properties more strongly than superlattices. The largest reduction in thermal conductivity is observed at 50% dot concentration, but the dot radius appears to have little effect on the magnitude of reduction around this concentration.

DOI: [10.1103/PhysRevB.86.115410](https://doi.org/10.1103/PhysRevB.86.115410)

PACS number(s): 61.46.-w, 65.80.-g, 68.65.-k, 66.70.-f

I. INTRODUCTION

Following the isolation of single-layer graphene,¹ studies on the electrical,²⁻⁶ optical,^{7,8} thermal,⁹⁻¹⁴ and mechanical^{15,16} properties of this low-dimensional material have revealed its potential for many technological applications.¹⁷⁻²⁰ This in turn has triggered interest in isomorphs of graphene, namely hexagonal boron nitride (*h*-BN)²¹⁻²⁸ and hybrid *h*-BN/graphene structures. Recently, fabrication of both random immersions of *h*-BN in graphene^{29,30} and well defined clusters of *h*-BN in graphene with possible kinetically controllable domain sizes³¹ has intensified this interest. In particular, such hybrid systems have a considerable compositional and structural diversity that translates into greater freedom for tuning the physical properties. Both experimental and density functional theory (DFT) studies have shown that the physical properties of these materials can be significantly modified by simply varying the relative amount of *h*-BN to graphene.³²⁻³⁴ For instance, Ci *et al.*³¹ have experimentally shown that decreasing the relative amount of *h*-BN to graphene increases the electrical conductivity, which has been supported by DFT studies where increasing BN concentration and cluster size results in band gap opening.^{35,36} It was recently shown that the details of the bonding at the *h*-BN/graphene interface can change the type of intrinsic doping of the

system.³⁷ There are other examples of how the chemical and structural diversity in this low-dimensional hybrid system enable control over magnetic properties; e.g., zigzag edges in ribbons have been suggested to lead to ferromagnetic behavior,³⁸ while more complex interfaces, such as those present in *h*-BN clusters embedded in graphene, can be antiferromagnetic.³⁹

Thermal transport in graphene with embedded *h*-BN quantum dots has been studied recently using a real-space Kubo approach.⁴⁰ This study has shown that the decreasing dot size decreases the phonon mean free path (MFP) of both in-plane and out-of-plane modes considerably. However, limited variation in MFP has been observed by changing the dot concentration at the smallest dot sizes. In another study, the effect of BN nanodots on the heat current in graphene nanoribbons has been investigated by using nonequilibrium Green's functions and nonequilibrium (direct method) molecular dynamics.⁴¹ The authors claimed that there is a linear inverse relationship between the number of atoms at the interface and the heat current. Although these studies provide valuable insight about the thermal transport, the thermal conductivity of graphene/*h*-BN nanostructured systems has not been investigated systematically by considering superlattices with different nano-morphologies. The objective

of this study is to investigate the influence of the chemical and structural diversity present in hexagonal boron nitride (*h*-BN) and graphene hybrid nanostructures on thermal transport and to test possible pathways for tuning the thermal conductivity of these low-dimensional hybrid structures. In this paper, we investigate the variation of thermal conductivity of hybrid graphene/*h*-BN nanostructures; in particular we study (1) stripe superlattice geometries while varying geometric parameters and composition and (2) BN (graphene) dots embedded in graphene (BN) as a function of dot-diameter and composition. The theoretical findings aim at providing basis for potential thermal management applications in miniaturized devices.

We have previously calculated the lattice thermal conductivities of nanotubes, graphene, and *h*-BN based nanostructures^{42–46} with considerable accuracy and compared the results with available experimental data.¹⁴ In this study, we implement an accurate model for C-B and C-N interactions by employing DFT calculations in addition to our previous *h*-BN potential. Using these Tersoff interatomic potentials, we calculated the lattice thermal conductivity of several possible graphene/*h*-BN hybrid structures. The rest of the report is organized as follows: First, the model utilized to develop the potential and the calculation methods for thermal conductivity are described. Then, the validity of our potentials for studying hybrid nanostructures is demonstrated. This is followed by a detailed description of the considered hybrid nanostructures and a discussion of the effect of structure and composition on lattice thermal transport properties.

II. METHOD

Equilibrium molecular dynamics simulations can be utilized to obtain instantaneous heat current (\mathbf{J}) or energy moment (\mathbf{R}) as a function of time. Subsequently, thermal conductivity κ can be evaluated by using either the heat current autocorrelation function (Green-Kubo method)^{47–49} or mean square displacement of the energy moment (Einstein relation)⁴⁹ as discussed in detail in our earlier studies.^{43–45,50,51} Here, the thermal conductivity is evaluated from the Einstein relation (the mean square displacement of energy moment, named *h*MSD) as given by⁵²

$$\frac{\langle [R_\mu(t) - R_\mu(0)]^2 \rangle}{2Vk_B T^2} = \kappa_{\mu\mu} [t + \tau(e^{-t/\tau} - 1)]. \quad (1)$$

Here, V is the volume, T is the temperature, and k_B is the Boltzmann constant. The energy moment through direction μ is defined by R_μ . The right-hand side of Eq. (1) represents a linear change in the Einstein relation for time (t) much larger than the decay time (τ). The long-time behavior corresponds to diffusive regime in transport of heat. For short times, on the other hand, the average energy propagation is ballistic and results in a nonlinear relation between κ and *h*MSD. Given the time, a bulk system assumes a diffusive behavior at elevated temperatures, and thus we are more interested in this regime.

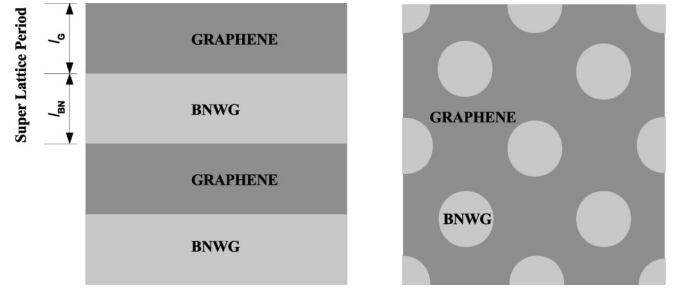


FIG. 1. The hybrid structures considered in this work, viz., stripe superlattices and dots embedded in a sheet matrix.

Computationally, we eliminate the nonlinear portion of the relationship by discarding the first 100 ps of *h*MSD then fit the rest to a linear function, i.e., $hMSD = 2Vk_B T^2 \kappa_{\mu\mu} t$, in order to obtain thermal conductivity.

In this study, we investigate the thermal conductivity of graphene/*h*-BN superlattices in the form of stripes and dots/“antidots”; see Fig. 1. The stripe superlattices are discussed in two general categories. In the first case periods are equal ($l_G = l_{BN}$), and in the second unequal periods ($l_G \neq l_{BN}$) of graphene and *h*-BN stripes are simulated. The stripes of graphene and *h*-BN sublattices are connected via two different orientations, resulting in a zigzag or an armchair interface. For all structures, approximately $60 \times 60 \text{ nm}^2$ periodic domains are considered. Previously, we showed that such large systems are required for the proper convergence of thermal conductivity in equilibrium MD calculations of ribbonlike systems.⁴³ For the equal-period simulations, in each orientation, five different period thicknesses ranging from ~ 1.25 to $\sim 30 \text{ nm}$ are constructed. The atomistic details of these systems are given in Table I in the Appendix. For the unequal-period simulations, again five different configurations are created for the armchair and zigzag interface systems where the thicknesses of BN sublattices change from ~ 3 to $\sim 57 \text{ nm}$ and the sum of l_{BN} and l_G is set to $\sim 60 \text{ nm}$; see Table II in the Appendix for details.

As a second type of nanostructure, dots of *h*-BN are embedded in graphene with a close-packed arrangement as shown in Fig. 1. We select three different radii (4.95, 12.38, and 24.76 Å) for these ordered dots. Ordered graphene dots in *h*-BN, so called antidots, are created with a radius of 12.38 Å. Random configurations of antidots are also considered with radii of 6.19 and 12.38 Å. The details of these structures are provided in Table III in the Appendix.

Molecular dynamics simulations are performed in the microcanonical ensemble with a time step of 1.0 fs to conserve energy and a simulation length of 5 ns to obtain an acceptable ensemble average of *h*MSD. Each data point for κ is therefore obtained by averaging the results of a minimum of five distinct simulations with different initial velocity distributions. The error in κ values is calculated from the standard deviation of these independent calculations. The volumes of the two-dimensional structures are defined as $lw\Delta$, where w and l are the width and the length of simulated structures, and Δ (0.335 nm) is the mean Van der Waals thickness for *h*-BN and graphene. Finally, we did not consider isotopic disorder

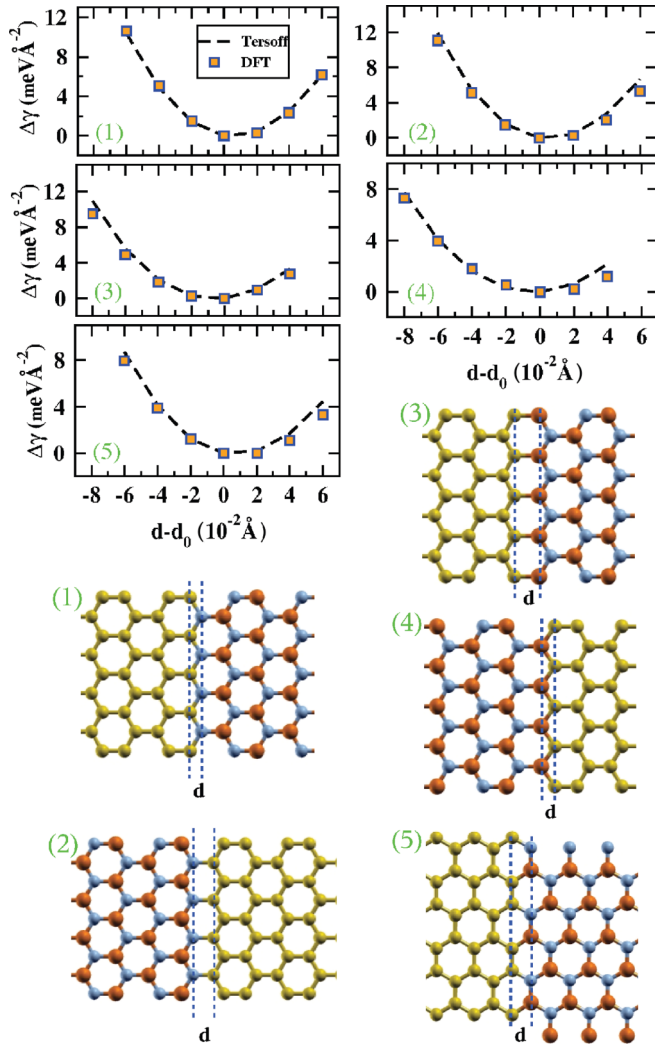


FIG. 2. (Color online) The change in the total energy, as given by both the Tersoff potential and DFT, per interface area as a function of interface separation d . The corresponding structures for the interfaces are given with ball-and-stick representations (C = yellow, N = small blue, B = big red atom).

explicitly in thermal conductivity calculations. Instead, a single mass of natural abundance is used for all elements.

We have previously developed a Tersoff-type potential for h -BN systems.⁴⁴ Also, a Tersoff parameterization for graphene is given by Lindsay and Broido.⁵³ Both potentials have been optimized to reproduce the DFT phonon dispersions for their respective materials, necessary for ensuring accurate lattice thermal conductivities. In order to simulate the interfaces, one needs to further develop interaction potentials for all possible element pairs coupling at the interface. We have used DFT calculations to generate the data needed for the interfaces. These calculations have been performed with the Vienna *ab initio* simulation package (VASP)^{54,55} which is based on density functional theory. A projector augmented wave (PAW)^{56,57} pseudopotential formalism was imposed with a Perdew-Burke-Ernzerhof (PBE)⁵⁸ form of generalized gradient approximations (GGA). Using DFT energetics to condition empirical potentials has been previously motivated for both pure graphene and h -BN. The PAW-PBE formalism,

in particular, produces accurate structures for our systems of interest, with the calculated lattice parameters for graphene and h -BN being 2.45 and 2.51 Å, respectively. Long horizontal strips of the structures in Fig. 2 are used in periodic-boundary conditions in order to avoid spurious interface-interface interactions. Depending on the basic repeating unit of the given structures, in-plane dimensions of 29.95×2.47 Å (structures 2 and 3), 30.22×2.49 Å (structures 1 and 4), or 24.8×4.30 Å (structure 5) were used with $2 \times 16 \times 1$, $2 \times 16 \times 1$, and $2 \times 10 \times 1$ Monkhorst-Pack k point grids, respectively. 400 eV is selected for the plane wave energy cutoff to achieve the energy convergence.

III. RESULTS AND DISCUSSIONS

A. Optimization of C-BN parameters

As pointed out in the previous section, reliable potentials for C-C and B-N interactions have appeared in the literature. To simulate the hybrid structures of interest, we must then only define the interactions between B-C and N-C. Since the structure and vibrational spectrum of h -BN and graphene are similar, we opt to employ the mixing rules and fitting procedure put forth by Tersoff for Si-Ge and Si-C,⁵⁹ which approximates the parameters as a mixture of the existing BN and C parameters modified by two arbitrary values, χ_{B-C} and χ_{N-C} . These parameters adjust the contribution from the attractive term to the potential. We have obtained χ_{B-C} and χ_{N-C} by imposing the requirement on the potential to reproduce DFT energetics of all probable h -BN/graphene interfaces shown in Fig. 2. In these graphs, $\Delta\gamma$ is the change in total energy per interface area (width \times Van der Waals thickness) as the interface separation d changes from the equilibrium value d_0 , under the condition that the bond lengths in the graphene and h -BN regions are held fixed. The corresponding interfaces are also shown in Fig. 2. Note that the interface separation parameter d accounts for both bond length and angle variations. Parameter fitting is accomplished by minimizing the differences between the DFT and the force field derived $\Delta\gamma$ values for each displacement for each structure simultaneously by updating the force field parameters using a genetic algorithm. The fitted parameters for χ_{B-C} and χ_{N-C} (0.886777 and 1.013636 respectively) along with the parameters obtained from the mixing rule have produced MD energies in good agreement with DFT results. Moreover, the error in the calculated equilibrium B-C and N-C bond lengths of all structures is no larger than 1.5%. A full list of parameters along with the description of interaction potential function and the mixing rules are given in Table IV of the Appendix.

B. Stripe superlattices with equal periods

In all striped superlattice structures, we calculated the lattice thermal conductivities parallel, κ_{\parallel} , and perpendicular, κ_{\perp} , to the superlattice orientation. The chosen interfaces are shown in Figs. 3 and 4 with the associated thermal conductivity values. The ball-and-stick structure in Figs. 3(a) and 4(a) is the same interface given in Fig. 2 as structure 5: essentially one armchair ribbon connected to the other two in

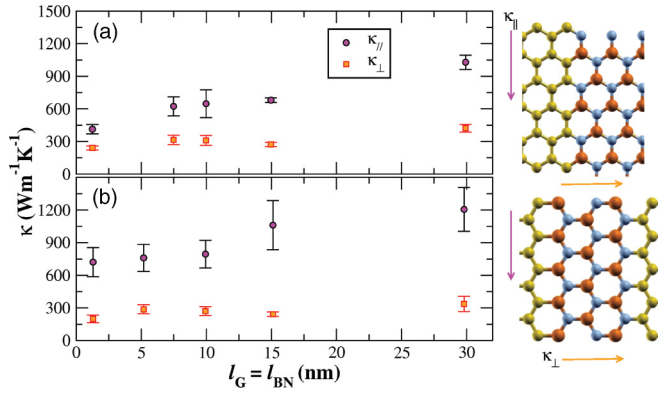


FIG. 3. (Color online) The thermal transport coefficients parallel and perpendicular to the two different graphene/*h*-BN interfaces are shown in (a) and (b). The period lengths of both graphene and *h*-BN are constrained to be equal. The atomistic details for the calculated structures are given in Table I in the Appendix.

a symmetrical fashion though forming B-C and N-C bonds. In contrast the structure represented as Figs. 3(b) and 4(b) can be thought of as one zigzag ribbon connected to two others on one side by B-C bonds and on the other by N-C bonds. These interfaces correspond to structures 2 and 3 in Fig. 2. The effective stiffness at the interface, obtained by fitting the $\Delta\gamma$ to a quadratic function, shows that the C-N bond is stronger than C-B bond. This is expected considering that both interactions are mainly covalent, and as more electrons are involved in the bonding, the strength of the bond increases.

Figure 3 shows how the thermal conductivity of the aforementioned superlattice interfaces behaves when the periods, constrained by $l_G = l_{BN}$, are varied. The transport coefficients in the parallel direction, however, behave differently, depending on the type of interface. The superlattice with the armchair interface has smaller thermal conductivity compared to the one with the zigzag interface in the studied period range. As the period thickness increases, the striped structures appear to

become less sensitive to interface effects on parallel thermal conductivity for both interfaces approaching 1050–1200 W/mK. This is close to the midpoint of the thermal conductivity values of pristine *h*-BN, 450 W/mK, and graphene, 2300 W/mK. This behavior agrees quantitatively with what is expected from treating the striped structure as the combination of two independent nanoribbons. Previously, it was shown that zigzag ribbons have better thermal transport properties than armchair ribbons at small widths because of the latter having higher atomic line density on the edge.^{43,44} Thicker ribbons have more transport channels, and the difference in scattering behavior at the edges become less significant. Thus, it is sensible for striped structures combined through zigzag interfaces to have larger transport coefficients in smaller periods. Another apparent observation is that the thermal transport coefficients perpendicular to the different interfaces behave similarly, gradually increasing from 200–250 W/mK at $l = 1.5$ nm to 350–400 W/mK at $l = 30$ nm. The perpendicular thermal transport is strongly controlled by the lower thermal conductivity component (*h*-BN) and the interface phonon scattering even at a 30 nm thickness. If one assumes that the periods of the stripes are longer than the phonon mean free path and the boundary resistance is negligible, then κ_{\perp} of the striped system of equal periods is bounded by $2(\kappa_{\text{graphene}} \times \kappa_{h\text{-BN}})/(\kappa_{\text{graphene}} + \kappa_{h\text{-BN}})$. For the calculated superlattices this equation gives 752.7 W/mK. The actual physics of the simulated systems, on the other hand, will not resemble the idealized picture. First, the system has a finite thermal boundary resistance that depends on the acoustic mismatch of the stripes and the intrinsic properties of the boundary. The effect of boundary structure on κ_{\perp} is less pronounced when the results from Figs. 3(a) and 3(b) are compared, and it is almost independent for zigzag and armchair interfaces. Second, some of the systems have period lengths of only few nanometers, which is very short compared to the MFP of the relevant phonons. Thermal conductivity perpendicular to the interface increases slowly as the period size grows; however, the ideal value will not be reached because of the limiting effect of thermal boundary resistance, which will be present even in systems with period sizes longer than the characteristic MFP.

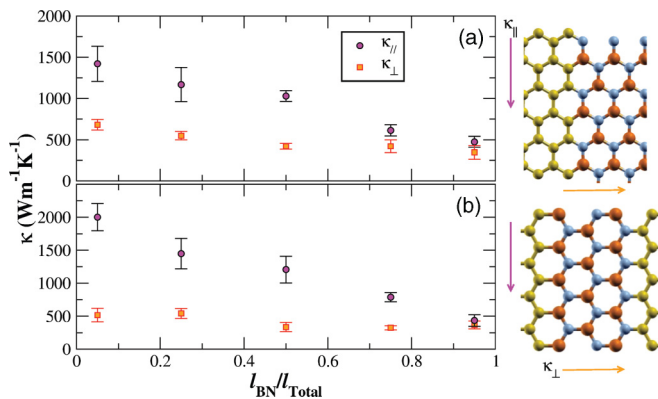


FIG. 4. (Color online) The thermal transport coefficients parallel and perpendicular to the two different graphene/*h*-BN interfaces are shown in (a) and (b). The sum of period lengths of graphene and *h*-BN are constrained to be 60 nm. The atomistic details for the calculated structures are given in Table II in the Appendix.

C. Stripe superlattices with unequal periods

Using the same interfaces, we remove the constraint of equal size periods and only require the sum of l_{BN} and l_G to be 60 nm. We note here that the variation of the period lengths also enables us to see the influence of concentration. When *h*-BN has a small concentration (or a small period), the parallel component of thermal transport increases toward the limiting value of graphene as seen in Fig. 4. On the other hand, the perpendicular component does not exceed 700 W/mK. Again, the zigzag interfaces have higher parallel thermal transport coefficients (35% larger) than the armchair interfaces in almost all configurations. When the period of BN is small, the reduction in κ_{\perp} from the pristine graphene value is mainly due to interfacial phonon scattering; systems with larger l_{BN} drive κ_{\perp} toward the pure BN values but are still limited by the influence of interfacial scattering. The effect of atomic bonding at the interface on conduction is most clearly seen when $l_{BN}/l_{\text{Total}} = 0.05$. Conductivity perpendicular to

the boundary in the armchair interface sample is noticeably higher than in the zigzag sample. This is most probably caused by enhanced scattering from alternating types of interface bonding in zigzag boundaries.

D. Dot and antidot superlattices

We now turn to the investigation of the thermal conductivity of ordered and random distributions of *h*-BN dots embedded in graphene. Figure 5 shows the influence of dot size and concentration on the κ . From Fig. 5 we see that larger dot sizes lead to higher thermal transport coefficients. At the lowest BN concentration (2%) the system with the largest dot has a 20% larger transport coefficient than the other sizes. This could be understood by the fact that larger dots have a smaller boundary-to-bulk ratio at the same concentration. As more dots are introduced, this interface effect is suppressed and the κ of all systems converge to 250 W/mK at 40% *h*-BN. Interestingly, this large concentration limit is similar to the perpendicular conductivity of stripe superlattices with periods similar to the diameter of the dots; see Fig. 3. It is likely that at large concentrations the *h*-BN dots can isotropically limit the thermal transport in the same manner that the stripes limit the transport perpendicular to the boundary.

In addition to ordered BN dots, we have modeled ordered and random distributions of graphene dots in *h*-BN. The thermal conductivity values of these systems are also presented in Fig. 5. A decreasing behavior in thermal conductivity is also observed in these systems as the number of graphene dots increases. It is surprising to see that graphene, as the higher κ component, does not enhance the thermal conductivity of *h*-BN. This can be attributed to the relatively small size of the dots

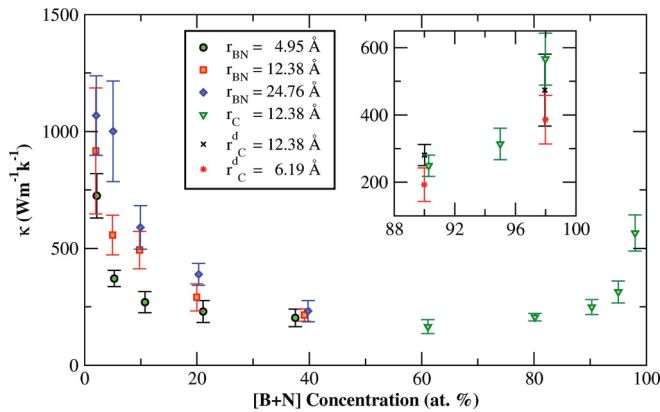


FIG. 5. (Color online) The thermal transport properties of graphene with embedded *h*-BN dots and *h*-BN with embedded graphene. Three different radii, 4.95, 12.38, and 24.76 Å are used for *h*-BN dots. The numbers of dots in the systems are varied such that the BN concentration ranges from 2% to 98%. Two different radii, 6.19 and 12.38 Å, are employed for graphene dots. The superscript “d” indicates the disordered dot arrangement. BN concentration on the horizontal axis is calculated as the percent ratio of the total number of boron and nitrogen atoms to the total number of atoms. The inset graph has the same axis units as the outer graph. The atomistic details for these systems are given in Table III in the Appendix.

and the large *h*-BN/graphene interface-to-area ratio, leading to interfacial phonon scattering events dominating κ . At the lowest C concentration, the ordered dot system has higher thermal conductivity than the bulk value of *h*-BN. It is not clear whether this is an actual physical phenomena or an averaging problem since the error bars are large enough to include the bulk value. In creating the random dot configurations, we maintain the mean dot separation similar to the one in the ordered configurations with the same concentration. For each concentration, the initial conditions of the simulations are not only varied by atom velocities but the also the distribution of the dots. The thermal conductivities of the structures, having ordered and random dots, are not significantly different for the same dot sizes and concentrations (see the inset of Fig. 5). Again, the smaller dots lead to lower κ when the concentration of C is kept constant.

IV. SUMMARY AND CONCLUDING REMARKS

We have characterized the lattice thermal transport properties of hybrid graphene and *h*-BN structures: graphene-white graphene stripes and dot/antidot superlattices. The κ_{\perp} of striped nanostructures with large periods is limited by the less conductive component, *h*-BN. The parallel transport, on the other hand, attains a value close to the average of the two components. As the periods of the stripes are reduced, interface scattering effects become more prevalent with zigzag interfaces resulting in higher κ than the armchair interfaces. The thermal conductivity of the dot systems can be tailored by both dot diameter and concentration. Small dot concentration and large dot diameter lead to larger conductivities. Moreover, the transport properties of nanosystems with high dot concentrations are independent of size, approaching the κ_{\perp} of the small-period stripe superlattices.

ACKNOWLEDGMENTS

We acknowledge support from the NSF (DMR 0844082) to the International Institute of Materials for Energy Conversion at Texas A&M University as well as AFRL. Parts of computations were carried out by the Laboratory of Computational Engineering of Nanomaterials, supported by ARO, ONR, and DOE grants. We would also like to thank the Supercomputing Center of Texas A&M University for a generous time allocation for this project. C.S. acknowledges the support from The Scientific and Technological Research Council of Turkey (TUBITAK) to his research at Anadolu University.

APPENDIX

Structural details of stripe and dot superlattices are given in Tables I–III.

The potential used in this study is developed by Tersoff:⁵⁹

$$V_{ij} = f_C(r_{ij})[f_R(r_{ij}) + b_{ij}f_A(r_{ij})],$$

$$f_C(r_{ij}) = \begin{cases} 1, & r_{ij} < R_{ij}, \\ \frac{1}{2} + \frac{1}{2} \cos\left(\pi \frac{r_{ij} - R_{ij}}{S_{ij} - R_{ij}}\right), & R_{ij} < r_{ij} < S_{ij}, \\ 0, & r_{ij} > S_{ij}, \end{cases}$$

TABLE I. Simulation details for the stripe superlattices where graphene and h -BN have equal period thicknesses. Thermal conductivities of these structures are given in Fig. 3. The total sizes of the systems are given by $\text{Length}_{\text{arm}}$ and $\text{Length}_{\text{zig}}$ where the subscripts define whether the length is measured along the armchair or the zigzag configuration.

Boundary \ Period (nm)	# of B	# of N	# of C	$\text{Length}_{\text{arm}}$ (nm)	$\text{Length}_{\text{zig}}$ (nm)
Armchair \ $l = 1.246854$	33 600	33 600	67 200	60.469 25	59.848 97
Armchair \ $l = 7.481121$	33 600	33 600	67 200	60.469 25	59.848 97
Armchair \ $l = 9.974828$	33 600	33 600	67 200	60.469 25	59.848 97
Armchair \ $l = 14.9622$	33 600	33 600	67 200	60.469 25	59.848 97
Armchair \ $l = 29.92449$	33 600	33 600	67 200	60.469 25	59.848 97
Zigzag \ $l = 1.2957698$	32 982	32 982	65 964	59.605 41	59.599 60
Zigzag \ $l = 5.1830792$	34 560	34 560	69 120	62.196 95	59.848 97
Zigzag \ $l = 9.934235$	32 982	32 982	65 964	59.605 41	59.599 60
Zigzag \ $l = 15.1173$	33 600	33 600	67 200	60.469 25	59.848 97
Zigzag \ $l = 30.234625$	33 600	33 600	67 200	60.469 25	59.848 97

TABLE II. Simulation details for the stripe superlattices where graphene and h -BN have different period thicknesses. Thermal conductivities of these structures are given in Fig. 4. The total sizes of the systems are given by $\text{Length}_{\text{arm}}$ and $\text{Length}_{\text{zig}}$ where the subscripts define whether the length is measured along the armchair or the zigzag configuration.

Boundary \ $l_{\text{BN}}/l_{\text{total}}$	# of B	# of N	# of C	$\text{Length}_{\text{arm}}$ (nm)	$\text{Length}_{\text{zig}}$ (nm)
Armchair \ 0.05	3360	3360	1 276 80	60.469 25	59.848 97
Armchair \ 0.25	16 800	16 801	1 008 00	60.469 25	59.848 97
Armchair \ 0.50	33 600	33 600	67 200	60.469 25	59.848 97
Armchair \ 0.75	50 400	50 400	33 600	60.469 25	59.848 97
Armchair \ 0.95	63 840	63 840	6720	60.469 25	59.848 97
Zigzag \ 0.05	3360	3360	1 276 80	60.469 25	59.848 97
Zigzag \ 0.25	16 800	16 800	1 008 00	60.469 25	59.848 97
Zigzag \ 0.50	33 600	33 600	67 200	60.469 25	59.848 97
Zigzag \ 0.75	50 400	50 400	33 600	60.469 25	59.848 97
Zigzag \ 0.95	63 840	63 840	6720	60.469 25	59.848 97

TABLE III. Simulation details for graphene with embedded h -BN dots and h -BN with embedded graphene antidots. Thermal conductivities of these structures are given in Fig. 5.

Radius (nm)	# of B	# of N	# of C	Length_x (nm)	Length_y (nm)
$r_{\text{BN}} = 0.495$	6000	4800	18 000	29.712 00	25.731 30
	3840	3072	25 856	31.692 80	27.446 80
	2016	1728	31 104	32.683 20	28.304 46
	960	768	31 040	31.692 80	27.446 76
	540	432	44 028	37.140 00	32.164 17
$r_{\text{BN}} = 1.238$	12 384	12 960	39 456	44.568 00	38.597 04
	5504	5760	45 184	41.596 80	36.023 88
	3096	3240	58 464	44.568 00	38.597 01
	1376	1440	53 632	41.596 80	36.023 88
	348	360	34 140	32.683 20	28.304 48
$r_{\text{BN}} = 2.476$	13 032	12 744	39 024	44.568 00	38.597 01
	5792	5664	44 992	41.596 80	36.023 88
	1448	1416	25 936	29.712 00	25.731 35
	1448	1416	53 584	41.596 80	36.023 89
	1448	1416	1 365 28	65.366 40	56.608 96
$r_{\text{C}} = 1.238$	14 000	13 500	17 500	37.140 00	32.164 20
	22 784	22 464	11 200	41.596 80	36.023 88
	29 340	29 160	6300	44.568 00	38.597 01
	26 864	26 784	2800	41.596 80	36.023 88
	68 320	68 256	2816	65.366 40	56.608 96
$r_{\text{C}}^{\text{d}} = 1.238$	26 750	26 820	5950	39.885 52	40.154 93
	29 150	29 145	1225	39.875 75	40.145 09
$r_{\text{C}}^{\text{d}} = 0.619$	26 795	26 765	5960	39.898 08	40.167 57
	29 160	29 160	1200	39.884 07	40.153 47

TABLE IV. The parameters of the Tersoff potential optimized for C-BN interactions. The atom X represents the bond-modifying element where all parameters are exactly the same whether it is C, B, or N.

Parameters	C B X	C C X	C N X	B C X	B N X	N B X	N C X
A (eV)	1386.78	1393.6	1386.78	1386.78	1380.0	1380.0	1386.78
B' (eV)	339.068 91	430.0	387.575 15 2	339.068 91 0	340.0	340.0	387.575 15 2
λ^I (\AA^{-1})	3.5279	3.4879	3.5279	3.5279	3.568	3.568	3.5279
λ^{II} (\AA^{-1})	2.2054	2.2119	2.2054	2.2054	2.199	2.199	2.2054
n	0.727 51	0.727 51	0.727 51	0.727 51	0.727 51	0.727 51	0.727 51
β (10^{-7})	1.5724	1.5724	1.5724	1.257 24	1.257 24	1.257 24	1.257 24
c	38 049	38 049	38 049	25 000	25 000	25 000	25 000
d	4.3484	4.3484	4.3484	4.3484	4.3484	4.3484	4.3484
h	-0.93	-0.93	-0.93	-0.89	-0.89	-0.89	-0.89
R (\AA)	1.85	1.80	1.85	1.85	1.90	1.90	1.85
S (\AA)	2.05	2.10	2.05	2.05	2.00	2.00	2.05

$$f_R(r_{ij}) = A_{ij} \exp(-\lambda_{ij}^I r_{ij}),$$

$$f_A(r_{ij}) = -B'_{ij} \exp(-\lambda_{ij}^{II} r_{ij}), \quad B'_{ij} = B_{ij} \chi_{ij},$$

$$b_{ij} = (1 + \beta_i^{n_i} \zeta_{ij}^{n_i})^{-\frac{1}{2n_i}}, \quad \zeta_{ij} = \sum_{k \neq i,j} f_C(r_{ik}) g(\theta_{ijk}),$$

$$g(\theta_{ijk}) = \left(1 + \frac{c_i^2}{d_i^2} - \frac{c_i^2}{[d_i^2 + (\cos \theta_{ijk} - h_i)^2]} \right).$$

In this description the lower indices i , j , and k mark the atoms where an i - j bond is modified by a third atom k . The potential parameters and their corresponding values are given in Table IV. The parameter χ_{ij} was used as a fitting parameter in

our study. For the mixing of parameters, the geometric mean is calculated for the multiplier parameters and the arithmetic mean is calculated for the exponential parameters. These rules are

$$\lambda_{ij}^I = (\lambda_i^I + \lambda_j^I) / 2, \quad \lambda_{ij}^{II} = (\lambda_i^{II} + \lambda_j^{II}) / 2,$$

$$A_{ij} = (A_i A_j)^{(1/2)}, \quad B_{ij} = (B_i B_j)^{(1/2)},$$

$$R_{ij} = (R_i R_j)^{(1/2)}, \quad S_{ij} = (S_i S_j)^{(1/2)}.$$

It should be mentioned that χ_{ij} modifies B_{ij} , which is obtained as a result of the mixing procedure. Here, we also note that the developed potential is not parameterized to represent N-N or B-B interactions, as can be seen from Table IV.

*tcagin@tamu.edu

¹A. K. Geim and K. S. Novoselov, *Nature Mater.* **6**, 183 (2007).²A. H. Castro Neto, F. Guinea, N. M. R. Peres, K. S. Novoselov, and A. K. Geim, *Rev. Mod. Phys.* **81**, 109 (2009).³K. S. Novoselov, A. K. Geim, S. V. Morozov, D. Jiang, Y. Zhang, S. V. Dubonos, I. V. Grigorieva, and A. A. Firsov, *Science* **306**, 666 (2004).⁴K. Wakabayashi, Y. Takane, and M. Sigrist, *Phys. Rev. Lett.* **99**, 036601 (2007).⁵Y. Zhang, Y. Tan, H. Stormer, and P. Kim, *Nature (London)* **438**, 201 (2005).⁶A. Cresti, N. Nemeç, B. Biel, G. Niebler, F. Triozon, G. Cuniberti, and S. Roche, *Nano Research* **1**, 361 (2008).⁷X. Xu, N. M. Gabor, J. S. Alden, A. M. van der Zande, and P. L. McEuen, *Nano Lett.* **10**, 562 (2010).⁸R. R. Nair, P. Blake, A. N. Grigorenko, K. S. Novoselov, T. J. Booth, T. Stauber, N. M. R. Peres, and A. K. Geim, *Science* **320**, 1308 (2008).⁹J. H. Seol, I. Jo, A. L. Moore, L. Lindsay, Z. H. Aitken, M. T. Pettes, X. Li, Z. Yao, R. Huang, D. Broido *et al.*, *Science* **328**, 213 (2010).¹⁰A. A. Balandin, S. Ghosh, W. Bao, I. Calizo, D. Teweldebrhan, F. Miao, and C. N. Lau, *Nano Lett.* **8**, 902 (2008).¹¹S. Ghosh, W. Bao, D. L. Nika, S. Subrina, E. P. Pokatilov, C. N. Lau, and A. A. Balandin, *Nature Mater.* **9**, 555 (2010).¹²W. Cai, A. L. Moore, Y. Zhu, X. Li, S. Chen, L. Shi, and R. S. Ruoff, *Nano Lett.* **10**, 1645 (2010).¹³C. Faugeras, B. Faugeras, M. Orlita, M. Potemski, R. R. Nair, and A. K. Geim, *ACS Nano* **4**, 1889 (2010).¹⁴A. A. Balandin, *Nature Mater.* **10**, 569 (2011).¹⁵C. Lee, X. Wei, J. W. Kysar, and J. Hone, *Science* **321**, 385 (2008).¹⁶M. Yamada, Y. Yamakita, and K. Ohno, *Phys. Rev. B* **77**, 054302 (2008).¹⁷Q. Yan, B. Huang, J. Yu, F. Zheng, J. Zang, J. Wu, B.-L. Gu, F. Liu, and W. Duan, *Nano Lett.* **7**, 1469 (2007).¹⁸Z. Li, H. Qian, J. Wu, B. L. Gu, and W. Duan, *Phys. Rev. Lett.* **100**, 206802 (2008).¹⁹A. Rycerz, J. Tworzydło, and C. W. J. Beenakker, *Nature Phys.* **3**, 172 (2007).²⁰M. Y. Han, B. Özyilmaz, Y. Zhang, and P. Kim, *Phys. Rev. Lett.* **98**, 206805 (2007).²¹A. Rubio, J. L. Corkill, and M. L. Cohen, *Phys. Rev. B* **49**, 5081 (1994).²²D. Golberg, Y. Bando, Y. Huang, T. Terao, M. Mitome, C. Tang, and C. Zhi, *ACS Nano* **4**, 2979 (2010).²³A. Nag, K. Raidongia, K. P. S. S. Hembram, R. Datta, U. V. Waghmare, and C. N. R. Rao, *ACS Nano* **4**, 1539 (2010).

- ²⁴Y. Shi, C. Hamsen, X. Jia, K. K. Kim, A. Reina, M. Hofmann, A. L. Hsu, K. Zhang, H. Li, Z.-Y. Juang *et al.*, *Nano Lett.* **10**, 4134 (2010).
- ²⁵D. Pacile, J. C. Meyer, Ç. Ö. Girit, and A. Zettl, *Appl. Phys. Lett.* **92**, 133107 (2008).
- ²⁶H. Zeng, C. Zhi, Z. Zhang, X. Wei, X. Wang, W. Guo, Y. Bando, and D. Golberg, *Nano Lett.* **10**, 5049 (2010).
- ²⁷C. Zhi, Y. Bando, C. Tang, H. Kuwahara, and D. Golberg, *Adv. Mater.* **21**, 2889 (2009).
- ²⁸Y. Lin, T. V. Williams, and J. W. Connell, *J. Phys. Chem. Lett.* **1**, 277 (2010).
- ²⁹L. Qin, J. Yu, S. Kuang, C. Xiao, and X. Bai, *Nanoscale* **4**, 120 (2012).
- ³⁰W.-Q. Han, H.-G. Yu, and Z. Liu, *Appl. Phys. Lett.* **98**, 203112 (2011).
- ³¹L. Ci, L. Song, C. Jin, D. Jariwala, D. Wu, Y. Li, A. Srivastava, Z. F. Wang, K. Storr, L. Balicas *et al.*, *Nature Mater.* **9**, 430 (2010).
- ³²Y. Liu, S. Bhowmick, and B. I. Yakobson, *Nano Lett.* **11**, 3113 (2011).
- ³³K.-T. Lam, Y. Lu, Y. P. Feng, and G. Liang, *Appl. Phys. Lett.* **98**, 022101 (2011).
- ³⁴M. Qiu and K. M. Liew, *J. Appl. Phys.* **110**, 064319 (2011).
- ³⁵B. Xu, Y. H. Lu, Y. P. Feng, and J. Y. Lin, *J. Appl. Phys.* **108**, 073711 (2010).
- ³⁶P. P. Shinde and V. Kumar, *Phys. Rev. B* **84**, 125401 (2011).
- ³⁷M. Kan, J. Zhou, Q. Wang, Q. Sun, and P. Jena, *Phys. Rev. B* **84**, 205412 (2011).
- ³⁸S. Okada and A. Oshiyama, *Phys. Rev. Lett.* **87**, 146803 (2001).
- ³⁹A. Ramasubramaniam and D. Naveh, *Phys. Rev. B* **84**, 075405 (2011).
- ⁴⁰H. Sevinçli, W. Li, N. Mingo, G. Cuniberti, and S. Roche, *Phys. Rev. B* **84**, 205444 (2011).
- ⁴¹Jin-Wu Jiang and Jian-Sheng Wang, *Europhys. Lett.* **96**, 16003 (2011).
- ⁴²J. Che, T. Çağın, and W. A. Goddard III, *Nanotechnol.* **11**, 65 (2000).
- ⁴³J. Haskins, A. Kinaci, C. Sevik, H. Sevinçli, G. Cuniberti, and T. Çağın, *ACS Nano* **5**, 3779 (2011).
- ⁴⁴C. Sevik, A. Kinaci, J. B. Haskins, and T. Çağın, *Phys. Rev. B* **84**, 085409 (2011).
- ⁴⁵C. Sevik, A. Kinaci, J. B. Haskins, and T. Çağın, *Phys. Rev. B* **86**, 075403 (2012).
- ⁴⁶C. Sevik, H. Sevinçli, G. Cuniberti, and T. Çağın, *Nano Lett.* **11**, 4971 (2011).
- ⁴⁷M. S. Green, *J. Chem. Phys.* **22**, 398 (1954).
- ⁴⁸R. Kubo, *J. Phys. Soc. Jpn.* **12**, 570 (1957).
- ⁴⁹R. Zwanzig, *Annu. Rev. Phys. Chem.* **16**, 67 (1965).
- ⁵⁰A. Kinaci, J. B. Haskins, and T. Çağın, *J. Chem. Phys.* **137**, 014106 (2012).
- ⁵¹J. B. Haskins, A. Kinaci, and T. Çağın, *Nanotechnol.* **22**, 155701 (2011).
- ⁵²D. A. Weitz, D. J. Pine, P. N. Pusey, and R. J. A. Tough, *Phys. Rev. Lett.* **63**, 1747 (1989).
- ⁵³L. Lindsay and D. A. Broido, *Phys. Rev. B* **81**, 205441 (2010).
- ⁵⁴G. Kresse and J. Hafner, *Phys. Rev. B* **47**, 558 (1993).
- ⁵⁵G. Kresse and J. Furthmüller, *Phys. Rev. B* **54**, 11169 (1996).
- ⁵⁶P. E. Blöchl, *Phys. Rev. B* **50**, 17953 (1994).
- ⁵⁷G. Kresse and D. Joubert, *Phys. Rev. B* **59**, 1758 (1999).
- ⁵⁸J. P. Perdew, K. Burke, and M. Ernzerhof, *Phys. Rev. Lett.* **77**, 3865 (1996).
- ⁵⁹J. Tersoff, *Phys. Rev. B* **39**, 5566 (1989).